Two-stage ionoacoustic range verification leveraging Monte Carlo and acoustic simulations to stably account for tissue inhomogeneity and accelerator–specific time structure – A simulation study

Sarah K. Patch[a)]
Department of Physics, University of Wisconsin-Milwaukee, Milwaukee, WI, USA

Daniel E.M. Hoff, Tyler B. Webb, and Lee G. Sobotka
Departments of Chemistry and Physics, Washington University, St. Louis, MO, USA

Tianyu Zhao
Department of Radiation Oncology, Washington University, St. Louis, MO, USA

(Received 4 June 2017; revised 6 October 2017; accepted for publication 31 October 2017; published 21 December 2017)

Purpose: Range errors constrain treatment planning by limiting choice of ion beam angles and requiring large margins. Ionoacoustic range verification requires recovering the location of an acoustic source from low frequency signals. *A priori* information is applied to stably overcome resolution limits of inverse acoustic source imaging in this simulation study. In particular, the accuracy and robustness of ionoacoustic range verification for lateral and oblique delivery of high-energy protons to the prostate is examined.

Methods: Dose maps were computed using GEANT4 Monte Carlo simulations via the TOPAS user interface. Thermoacoustic pulses were propagated using k-Wave software, with initial pressures corresponding to instantaneous dose deposition and piecewise constant maps of tissue properties derived from the planning CT. A database of dose maps with corresponding thermoacoustic emissions and Bragg peak locations, referred to as "control points," were precomputed. Corresponding thermoacoustic emissions were also precomputed. Pulses were recorded at four coplanar locations corresponding to the outer surface of a virtual transrectal array. To model experimental beam delivery, k-Wave results were convolved in time with a Gaussian envelope to account for noninstantaneous proton delivery by a synchrocyclotron. Thermoacoustic pulses were bandlimited below 150 kHz, and amplitudes were directly proportional to charge delivered. To test robustness of our method, white noise was added. Range was estimated in a two-step process. The first step obtained a preliminary range estimate by one-way beamforming. The second step was taken using data corresponding to the "control point" nearest to the preliminary range estimate. For each receiver, the time of flight difference, Δt, between the measured and control thermoacoustic signals were accurately estimated by applying the Fourier shift theorem. Receiver-Bragg peak distance was then estimated by adding $v_s \Delta t$ to the known distance of the control point, where v_s is soundspeed. A linear system of equations based upon all receiver locations and distances was solved to recover the Bragg peak location. All simulations were performed relative to the planning CT. Because ultrasound (US) images were not available, results were overlaid onto the planning CT.

Results: Beamformed estimates from noise-free data tracked all beam locations within 1 cm. Final estimates for oblique and lateral beams were accurate to within 1.0 and 1.6 mm respectively. Average errors of final range estimates for oblique beams from data with SNR = 0 dB were no greater than 2.0 mm.

Conclusions: Ionoacoustic range verification may improve current practice. Ionoacoustic range estimates can be inherently co-registered to ultrasound images of underlying anatomy. To ensure estimates are robust in clinical practice, dose maps based upon the planning CT should be overlaid onto ultrasound volumes acquired at time of treatment and acoustic simulations re-computed to provide a database of control points and corresponding thermoacoustic emissions. Computation times for beamformed estimates are already fast enough for online range verification, but are not accurate enough for a measurement aperture limited to the surface of a transrectal ultrasound probe. Accelerated acoustic simulations will be required to enable online two-stage correction, but offline calculation is already suitable for adaptive planning.
[https://doi.org/10.1002/mp.12681]

Key words: IGRT, ion therapy, proton therapy, range verification

1. INTRODUCTION

Proton beams deliver maximal dose to tissue within a small region defined by the Bragg peak, whereas X-ray photon beams deliver an exponentially decaying dose along the beam path, dosing healthy tissue proximal and distal to the tumor. Proton therapy delivers less dose to proximal tissue, and spares distal tissue – if the beam alignment and range are correct. Because the dose gradient is steep near the Bragg peak, proton therapy is more sensitive than x-ray radiation therapy to positioning errors, day-to-day changes in anatomy and patient motion. Although interlocks halt treatment immediately upon detecting equipment failure, no safety mechanism exists to defend against anatomical changes and patient motion. Entire fractions are incorrectly delivered for lack of online range verification. Therefore, proton treatment plans often favor beam angles that are robust to range errors over plans that minimize overall collateral damage to healthy tissue.

Evidence-based medicine supports the use of current proton therapy protocols in tumors near the base of the neck, spine, eye and in pediatric patients,[1] but inadequate range verification otherwise limits clinical utility of proton therapy.[2] *In-vivo* range verification with a passive scatter system has been proposed by intentionally overshooting and irradiating radiosensitive tissue with a 3–5 cGy scout beam in order to correlate direct dose measurements by detectors embedded on the stabilization device with modulation wheel timing.[3] However, this method is only valid for pretreatment verification with selected beam angles. Its accuracy could be compromised severely by the location of the detectors. Another approach employs PET images derived from induced positron emitters from nuclear reactions induced by proton beams.[4] The PET image overlaying anatomy in CT images is a good indicator of delivered radiation to patients.[5] However, due to the decaying nature of the isotopes and the limits on PET imaging resolution, post-irradiation PET imaging is unable to achieve real-time imaging with millimeter accuracy. Prompt gamma emissions[6–13] can provide fast and real-time feedback, respectively, but cannot yet achieve millimeter accuracy. In addition, range is acquired in room coordinates, and is subject to setup uncertainty and intra-fractional motion when registered to underlying anatomy. MRI guidance provides real-time soft tissue visualization and handles setup uncertainty and intra-fractional motion for radiation therapy,[14,15] but does not address range verification during ion therapy.

Ionoacoustics offers the potential of online range verification with seamless and robust real-time correlation with anatomy visualized by ultrasound. The planning CT is acquired days before treatment and does not represent daily changes in anatomy, setup error, or intra-fractional motion. Real-time correlation of the Bragg peak location is only possible with an *in-vivo* imaging modality like ultrasound. We envision clinical implementation in a system similar to Elekta's Clarity, with multiple ultrasound transducers for suitable tumor sites, including prostate, liver, and perhaps pancreas.

Online range verification could augment ultrasound-based automated beam gating systems by acquiring both thermoacoustic emissions and ultrasound pulse-echoes and overlaying the Bragg peak onto live ultrasound (US) images. Whenever the delivered and planned treatment spot locations deviate by more than a preordained threshold the system would transmit a trigger signal to halt ion delivery. Potential benefits of online range verification include more aggressive treatment planning as well as hypofractionation. Accurate range verification would allow medical physicists to reduce treatment margins and enable adaptive treatment planning to compensate for modest range errors experienced during a previous fraction.

This study considers prostate cancer treatment, but ionoacoustic range verification could be applied to other tumor sites that can be visualized by ultrasound during treatment.

Approved protocols for prostate cancer treatment are extremely conservative and could be vastly improved by accurate range verification. To spare radiosensitive rectal tissue treatment is typically delivered laterally; beams travel through thick bony structures that introduce range uncertainty. Oblique delivery minimizes the proton path through bone and spares both bladder and rectum, but is sensitive to range errors because overshooting grazes the rectum. Ionoacoustic range verification could be performed using transrectal ultrasound arrays, overlaying the Bragg peak location on grayscale ultrasound images acquired by the same transducer.

The recent proliferation of proton therapy centers has spurred a renewed interest in ionoacoustic range verification. Basic science experiments performed at national laboratories in the 1970s[16,17] transitioned to clinically driven benchwork[18] and clinical testing[19] by the 1990s. Recently, measurements by individual receivers with lateral[20] and distal[21] offsets from the Bragg peak were simulated with an eye towards range verification. A mathematically complete set of measurements including both lateral and distal offsets was simulated to demonstrate feasibility of dosimetry for ion therapy,[22] and for x-rays.[23,24] Thermoacoustic emissions from 20 MeV pulses as short as 8 ns duration and microsecond-duration pulses of protons with energies exceeding 200 MeV into water baths have been detected using single element piezoelectric transducers[25,26] and hydrophones[27,28] respectively. Ionoacoustic range verification by overlaying the Bragg peak on an ultrasound (US) image[29] was performed using 50 MeV protons. The recent review[30] expands upon this summary.

Ionoacoustic range verification shares similarities with photo- and thermo-acoustic imaging, but differs in important ways. All thermoacoustic techniques rely upon temperature fluctuations to induce pressure changes. Pulsed electromagnetic irradiation using optical, microwave, and very high frequency (VHF) bands have been used for photoacoustic and thermoacoustic imaging of induced tissue heating. Pulsed delivery of x-ray and ion beams has been proposed for dosimetry and verification of beam position. Ionoacoustic signal encodes the stopping power profile terminating in a Bragg peak, which allows for range verification, whereas

photo- and thermoacoustic signals encode dielectric properties.

Ionoacoustic range verification is a natural consequence of the conversion of deposited dose to mechanical pressure pulses. Dose is quantified in Grays, 1 $Gy = 1\ J/kg$, whereas pressure is quantified by Pascals, 1 $Pa = 1\ N/m^2 = 1\ \mathrm{J}/m^3$. Assuming dose is deposited instantaneously, induced thermoacoustic pressure is given by

$$\delta p = \Gamma \rho D \tag{1}$$

where D is the dose delivered, Γ is the dimensionless Grüneisen parameter, and ρ is target density.

Optimal conditions for all thermoacoustic techniques include fast dose deposition satisfying stress confinement, ensuring pressure builds up faster than it can propagate away. The essential bandwidth of thermoacoustic emissions is limited by the inverse of the pulse duration. Anastasio, et. al. assumed constant soundspeed, v_s, and applied standard Green's function techniques to direly relate frequency content of the reconstructed volume, A, to temporal spectra of thermoacoustic measurements, $\mathbf{F}p(\mathbf{x},\omega)\cdot\mathbf{F}A(\mathbf{k})$ is a weighted integral of $\mathbf{F}p(\mathbf{x}, |\mathbf{k}| v_s)$ and its normal derivative over a general measurement aperture surrounding the support of A.[31] Therefore, when soundspeed is constant, bandlimitations on thermoacoustic measurements explicitly bandlimit thermoacoustic images.

Fortunately, range verification requires recovering only one number, location along the beam trajectory, rather than an N^3 volume of voxel values. Therefore, range verification can overcome the standard imaging requirements for high-resolution and artifact-free data reconstruction. On the other hand, range estimation by identifying the point at which the tomographic reconstruction achieves its maximum is sensitive to noise, particularly when limited angle data from only a few transducers data are available for beamforming. Recently, submillimeter range accuracy for a high energy proton beam was achieved by excessive averaging to improve the signal to noise ratio (SNR).[28]

Physical and biological challenges to ionoacoustic range verification include proton range straggling and the therapeutic dose limit.

Hardware and clinical limitations to ionoacoustic range verification are softening, however. Monte Carlo simulations using pencil beam parameters at 230 MeV yield dose in a water bath to be on the order of 1 cGy/pC, which increases pressure by 1 Pa/pC at the Bragg peak, assuming instantaneous deposition. Synchrocyclotrons deliver ions in pulses with 5–10 μs full width at half maximum, and are approaching the stress-confinement criteria for efficient thermoacoustic signal generation. IBA's S2C2 synchrocyclotron system routinely delivers 4–5 pC in less than 10 μs,[32] and the pulse duration of Mevion's S250 is 6 μs at low beam current. Hypofractionated protocols deliver more pulses to a treatment spot so more signals can be averaged to improve SNR.

We present a two-stage method to robustly and accurately estimate range from low frequency thermoacoustic emissions despite tissue heterogeneity and noise. The first stage sets the range estimate at the point at which the beamformed volume achieves its maximum, but the second stage triangulates using accurate estimates of transducer-to-Bragg peak distances. Rather than deconvolve the pulse envelope[33] we correlate noisy data to noise-free control data to accurately estimate distance between transducers and the Bragg peak. Distances between control Bragg peak locations and transducer locations are known; time of flight differences between control and measured data are accurately estimated from low frequency signals. This *in silico* study overlays results onto the planning CT and simulates both noisy measured data and noise free control data by assuming the same piecewise constant tissue properties: soundspeed, density, and Grüneisen. In practice, tissue properties are unknown, so to ensure accurate co-registration of range estimates to ultrasound images control data should be simulated using the same soundspeed assumed by the ultrasound scanner.

2. METHODS

2.A. Beam arrangement

A treatment plan was made with Eclipse 13.7 (Varian Medical System, Palo Alto, CA, USA) software with five beam angles to deliver full prescription dose to the prostate. The treatment plan consisted of two lateral beams, two anterior oblique beams at gantry angle 48 degrees and 312 degrees, and one anterior beam, as depicted in Fig. 1. All beams were coplanar. The detailed parameters were listed in Table I for all beams in the plan. The dose to the prostate was 79.4 Gy (relative biological effectiveness [RBE]) in 44 fractions. A factor of 1.1 was used to convert physical dose to RBE dose. The plan was optimized to deliver the prescription dose to at least 99% of the clinical target volumes and the volumes receiving 110% of the prescribed dose were less than 1%. Organs at risk included in plan optimization with 3.5% + 3 mm range uncertainty were the bladder, rectum and femoral heads. 0.35 mm × 5 mm gold Visicoil fiducials were permanently implanted and accounted for in the dose calculations.[34]

2.B. Monte Carlo simulation

Simulation was run on TOPAS (TOolkit for PArticle Simulation[35]) version 3.1, a user-friendly extension of Geant4. CT numbers were converted to mass density and elemental weights of tissues in four sections on the CT number scale by interpolating 71 human tissues.[36] One million histories were simulated for each single beam spot with 1 mm step size. Runtime for each beam simulation was 10 min on a workstation equipped with four AMD Opteron 6376 2.3 GHz 16 MB 16-core CPU and 256 GB memory. The dose grid discretization was set to 1 mm × 1 mm × 1 mm, to match the planning CT. All particles descending from primary protons, including secondary protons, electrons, photons, and neutrons were tracked and scored. Secondary particle generation was cut off at residual range of 0.05 mm for all media. Two

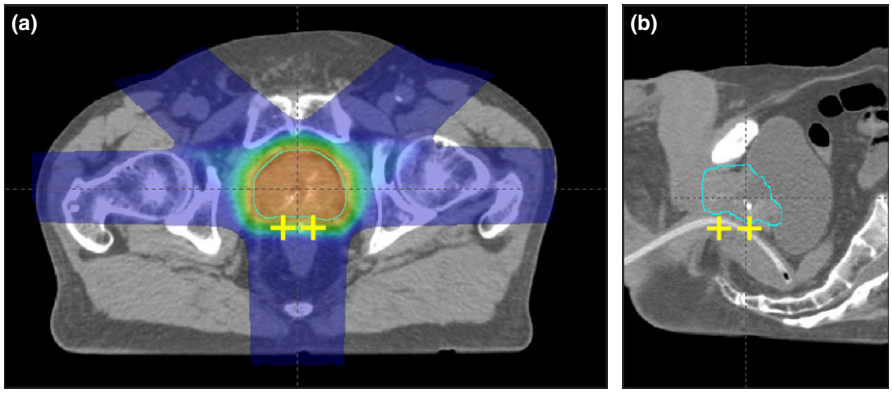

FIG. 1. Dose distribution in the prostate plan with approximate locations of low frequency acoustic receiver elements indicated by yellow "+." (a) axial plane. (b) sagittal plane. [Color figure can be viewed at wileyonlinelibrary.com]

TABLE I. Beam parameters in the prostate plan.

Beam	Angle (degrees)	# Layers	# Spots	Energies (MeV)
1	90	13	760	146.7–188.9
2	48	15	756	116.1–168.8
3	312	14	745	113.5–161.4
4	270	15	713	145.2–194.4
5	180	13	777	107.7–149.2

beam spots, one in the lateral field with gantry angle 90 degrees and another in the oblique field with gantry angle 48 degrees, were selected for beamformed range estimates in this study. The nominal energies of the two spots were 154.2 MeV and 139.2 MeV respectively. The spot size (1 σ) in air was 4 mm. Energies in the two beam spots were then altered deliberately in increments of 5 mm water equivalent thickness (WET) to simulate scenarios of under- or overshoot of protons that might occur during treatment, as detailed in Table II, where LR, AP, and SI represent left-right, anterior-posterior, and superior-inferior orientations.

2.C. k-Wave acoustic simulation

The k-Wave acoustics toolbox version 1.0 for Matlab (Mathworks, Natick, MA, USA) was used to propagate thermoacoustic emissions in three-dimensional space utilizing the pseudospectral method.[37] To minimize computational requirements, the CT volume was cropped in the LR and AP directions to minimize air surrounding and couch below the patient, and also in the SI direction, retaining 6 cm above and below the beam trajectories, which ran in axial planes. Dose maps were cropped to match the 200 × 320 × 144 voxel CT volume. All computations were performed on the same spatial grid as the planning CT and dose maps, padded by k-Wave's default 10-voxel matching layer. The acoustic source was computed by first assuming instantaneous proton delivery and then convolving by a proton pulse envelope measured described in subsection 2.D. Thresholding was applied to the planning CT to classify voxels into four material types: air, fat, bone, and muscle or organ. Representative values of soundspeed were selected from Table 4.2 in Duck's text[38] to create the soundspeed map in Fig. 2(a) and detailed in Table III. Similarly, representative values for density, specific heat capacity, and thermal expansion coefficient were used to create the multiplicative factor $\rho\Gamma$ displayed in Fig. 2(b). Figure 2(c) displays pressure induced by instantaneous delivery, computed by multiplying the Monte Carlo dose map by $\rho\Gamma$, as in Eq. (1). Soundspeed of bone and multiplicative factor of $\rho\Gamma$ was applied to Visicoil fiducials. Acoustic attenuation was not incorporated in the modeling.

TABLE II. Parameters for beamlets analyzed for range verification.

Name	Angle (degrees)	Bragg pk location (LR AP SI)	Type
Oblique 2	48	(−1 7 118)	Control
Oblique 3	48	(2 4 118)	Measured
Oblique 4	48	(5 1 118)	Control
Oblique 5	48	(8 −2 117)	Measured
Oblique 6	48	(11 −5 118)	Control
Oblique 7	48	(14 −7 118)	Measured
Oblique 8	48	(17 −10 118)	Control
Lateral 1	90	(11 2 111)	Control
Lateral 2	90	(7 2 112)	Measured
Lateral 3	90	(3 2 110)	Control

Emissions propagated for 75 μs, ensuring that the pulses traveled at least 110 mm and reached the virtual point receivers. To satisfy the Courant-Friedrichs-Lewy condition, k-wave established a temporal stepsize of $\Delta t = 93.75$ *ns* and propagated thermoacoustic emissions over 800 time steps. Computations were run on a MacPro with two 3.06 GHz 6-Core Intel Xeon with 32 GB of memory running Matlab R2017a with the parallel computing toolbox. No effort was made to optimize the code and runtimes were approximately 33 min per beamlet.

Pressures were recorded at four coplanar locations defining a 15 mm square in a coronal plane, corresponding to locations at which receive elements could be incorporated onto the form factor of a transrectal imaging array. The AP coordinate of all four virtual receive elements was 28 mm. LR coordinates were 0 and 15 mm; superior-inferior (SI) coordinates were 104 and 119 mm. Orthogonal projections of receive elements onto CT images are denoted by yellow "+"

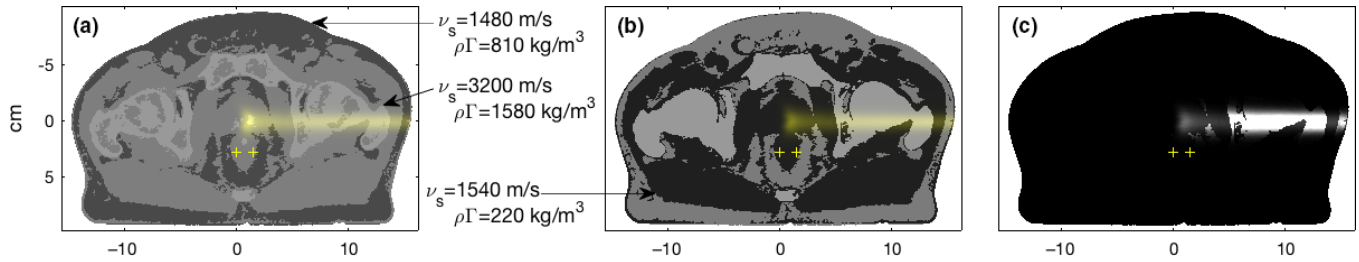

FIG. 2. Simulation parameters with lateral beams overlaid. Beam in (b) has energy of 154.2 MeV; water equivalent paths increase by 5 mm, for beams a–c. Beam dose is overlaid on soundspeed and $\rho\Gamma$ in subfigures (a) and (b), respectively. Initial pressure is displayed for beam (c). [Color figure can be viewed at wileyonlinelibrary.com]

TABLE III. CT numbers and corresponding tissue parameters.

Tissue	HU range	SOS (m/s)	Γ	ρ (kg/m^3)
Air	$(-\infty, -200)$	343	0.376	1.2
Fat	$(-200, -50)$	1480	0.877	920
Muscle, organ	$(-50, 100)$	1540	0.208	1040
Bone	$(100, +\infty)$	3200	0.788	2000
Visicoil fiducials	$(100, +\infty)$	3200	0.208	1040

in Fig. 2. Assuming instantaneous dose delivery, emissions recorded at the virtual transducer location at (LR, AP, SI)=(0, 28, 119) mm are plotted in Fig. 3(a) for oblique and lateral beams offset by 5 mm WET. Maxima achieved before 25 μs are due to the Bragg peak; maxima achieved after 30 μs were generated at bone-muscle interfaces. Figure 3(b) shows signals measured simultaneously by all four channels.

2.D. Experimental error models – Synchrocyclotron proton delivery and white noise

To demonstrate the robustness of our method two experimental effects were simulated. Noninstantaneous ion delivery was modeled using a proton pulse envelope measured during low-current delivery by a Mevion S250. White noise was added with varying amplitudes.

The temporal envelope of the proton beam delivered by a Mevion S250 proton therapy system was measured using a 1 mm × 1 mm × 6″ scintillating fiber attached to a photomultiplier tube (PMT). The 1 m × 1 mm face of the scintillating fiber was glued to a light guide on the end of a R1668 (1″) Hamamatsu PMT. The 1 mm × 6″ face was placed in the path of the beam. The waveforms were collected by a Tektronix DPO 4054 digital oscilloscope and analyzed offline. We triggered on the injection of hydrogen into the synchrocyclotron and observed proton pulses ~670 μs later. We lowered the beam intensity until only a few proton pulses were recorded with each trigger. Each pulse corresponds to individual/few proton events in the scintillator. We added 400 of these waveforms together to get a full profile of the beam. The profile was inverted, rebinned, and then fit to a Gaussian giving a FWHM of 5.8 μs, shown in Fig. 4(a).

To model the effect of non-instantaneous ion delivery, thermoacoustic pressures produced by k-Wave were convolved in time with a Gaussian with FWHM of 6 microseconds, resulting in smoothed plots in Fig. 3(c), reducing the impact of discontinuities generated at bone-muscle interfaces. Emissions from lateral beams became distinguishable, although they were not as well separated as smoothed emissions from oblique beams.

White noise was then added using Matlab's "randn" function and scaled to provide varying signal to noise ratios. SNR was defined in terms of the standard deviations, $SNR = 20\ \log_{10}(\sigma_{signal}/\sigma_{noise})$, for two reasons. Firstly, the time average of thermoacoustic pulses measured outside the support of the acoustic source is zero, so the standard deviation is proportional to the L^2 norm. Secondly, peak signal

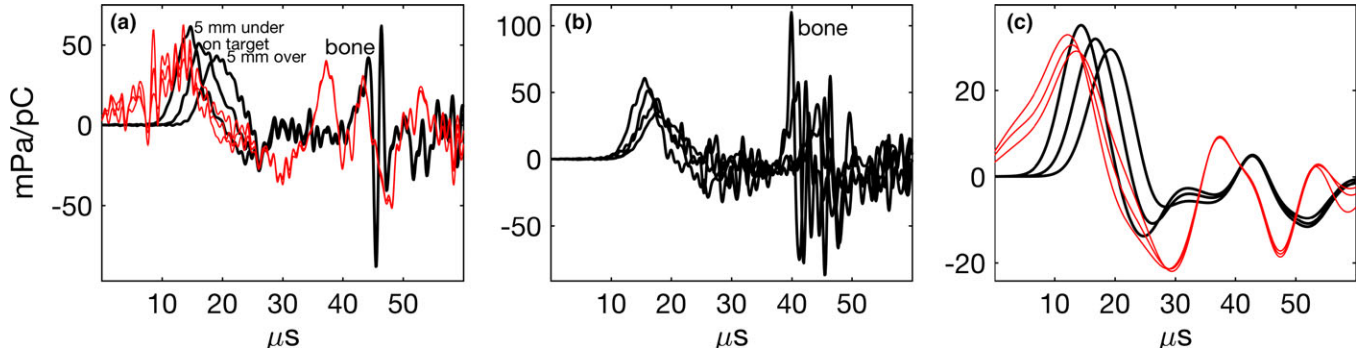

FIG. 3. Thermoacoustic emissions comparing ion pulse duration, beam range, and transducer locations. (a) Emissions due to instantaneous deposition from oblique and lateral beams in solid black and dashed red, respectively. (b) Emissions due to instantaneous deposition measured by all four single elements for an oblique beam. (c) Emissions from oblique and lateral beams, assuming a Gaussian time envelope with FWHM = 6 μs. [Color figure can be viewed at wileyonlinelibrary.com]

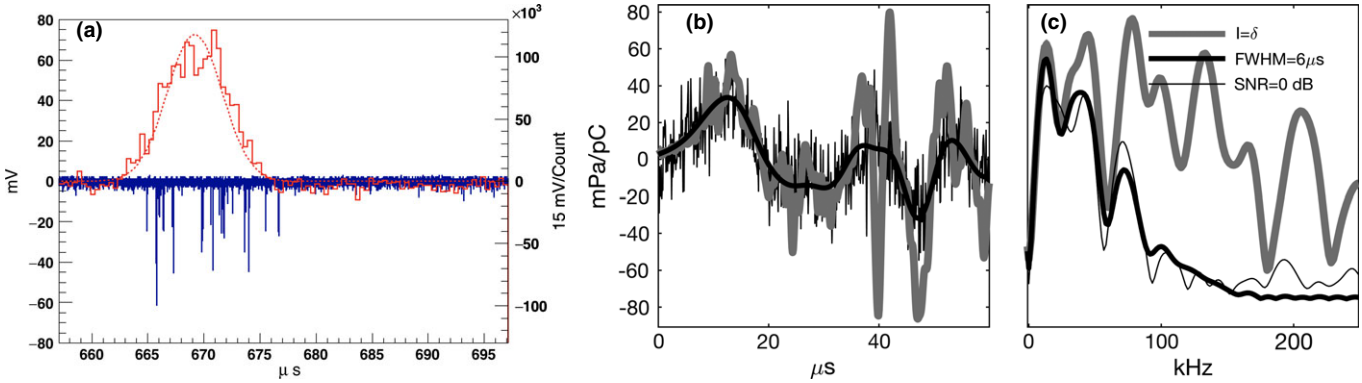

FIG. 4. (a) PMT signal from a single extraction showing individual hits on the scintillating fiber (blue), envelope from 400 extractions after inversion (solid red) with fitted Gaussian (dashed red). Simulated thermoacoustic emissions (b) and spectra (c) from lateral beam #2. [Color figure can be viewed at wileyonlinelibrary.com]

was typically from bone, rather than the prostatic tissue of interest. Range estimates were computed from 256 independent realizations to determine average range errors. Throughout this paper, results displayed for noisy data are for the first realization if not explicitly stated as average values. In Fig. 4(b), noise-free emissions corresponding to impulsive and experimental proton delivery are plotted with thick gray and black lines respectively. Adding white noise created the SNR = 0 dB realization plotted with a thin black line. Note that peak signals generated in the prostate (t <25 μs) are closely aligned in the thick noise-free curves in Fig. 4(b), but that adding noise can shift the peak location by more than a microsecond. Similarly, small errors in beamformed volumes shift range estimates.

2.E. Data preprocessing

Spectra plotted in Fig. 4(c) demonstrate that noise-free thermoacoustic emissions were bandlimited below 1/6 μs =160 kHz. Therefore, a Tukey window that transitioned to zero over 200–300 kHz was applied to lowpass filter the data. Resulting thermoacoustic signal and spectra are plotted with dashed lines in Figs. 4(b)–4(c).

Assuming instantaneous dose delivery one-way beamforming of data collected over a very small measurement aperture is essentially limited angle tomographic backprojection. Reconstructing the induced thermoacoustic pressure rise from complete data requires applying a differential operator prior to backprojecting.[39,40] Backprojection integrates over the measurement aperture and a complete measurement aperture is a two dimensional surface surrounding the region of interest. Integration and differentiation are inverse operations, and mathematically exact reconstruction balances the differential and integral operations. However, our measurement aperture is limited to a 2.25 cm^2 square, so rather than applying a first order differential operator, each time series was integrated prior to beamforming.

2.F. Range estimation

Range was estimated in two steps. The first step was computed quickly by backprojecting, or one-way beamforming, preprocessed measured emissions from transducer locations to obtain an initial "beamformed" estimate. The second step refined beamformed estimates by solving a triangulation problem with accurately computed transducer-to-Bragg peak distances, rather than beamforming low frequency signals. The second step required *a priori* knowledge of a database of thermoacoustic emissions simulated from Monte Carlo + acoustic software for multiple beams of varying energies.

2.F.1. First step

Fast backprojection/one-way beamforming of filtered thermoacoustic emissions throughout the 3D volume, assuming soundspeed of 1540 m/s, resulted in a low frequency function. The point at which the maximum was achieved was taken as the initial range estimate, indicated with yellow triangles in Fig. 5.

2.F.2. Second step

Preprocessed emissions from oblique beams #3, 5, 7, and 16 are referred to below as "measured" data. Noise-free preprocessed emissions and true Bragg peak locations for beams #2, 4, 6, 8, 14, and 16 were taken to be "control data" and "control points." Bragg peak locations for "control" beams and "measured" oblique beam #5 are plotted with magenta squares and dots in Fig. 6. Distances from the transducer locations to "control" Bragg peak locations were therefore known. For each set of measured data, the control location closest to the initial beamformed estimate was determined and the corresponding control data was used to refine the initial estimate.

For each measured emission, the time shift relative to its control emission was computed as follows. Measured and control signals were nulled for all time after onset of rarefaction to emphasize the initial thermoacoustic pressure increase used to compute time-of-flight. The Fourier shift theorem was applied to estimate time shifts between the noisy and control emissions by fitting a straight line to phase shifts in the low frequency Fourier components with amplitudes exceeding 10% of the DC component. Comparing two time series with hundreds of points robustly yielded a single

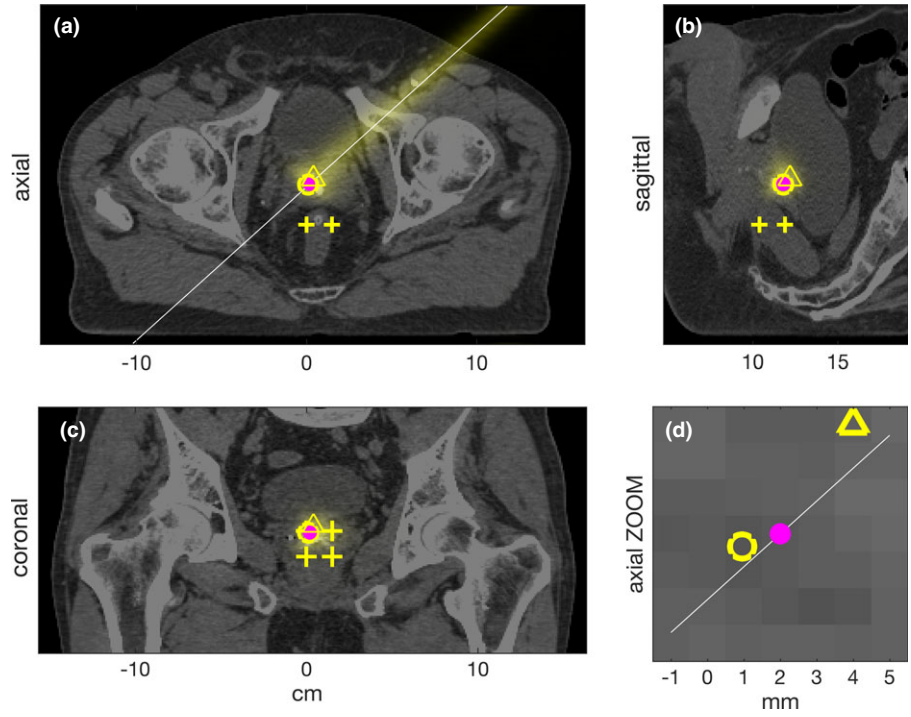

FIG. 5. TOPAS simulations of oblique beam and range estimates from SNR=0 dB signals overlaid on planning CT for oblique beam #3. "+" indicate locations of VLF receive elements projected orthogonally onto the CT plane. Axial, sagittal, and coronal planes through true Bragg peak location in (a) through (c), respectively. White line in (a) and (d) indicates beamline. Magenta dot is true Bragg peak location. Yellow triangle and circle indicate orthogonal projections of beamformed and final estimates. (d) Zoomed image of axial plane near Bragg peak. CT display window is [−200, +200] HU. [Color figure can be viewed at wileyonlinelibrary.com]

estimate for the time shift between them. Assuming constant soundspeed, the known distance between transducer k and the control Bragg peak location, d_k, was updated with time shifts, to more accurately estimate transducer to Bragg peak distances, $D_k = d_k + v_s\ \delta t_k$, where δt_k represents the time shift corresponding to transducer k.

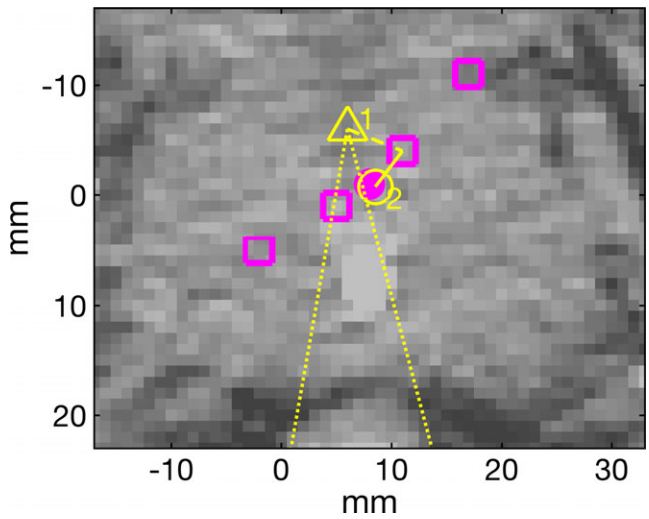

FIG. 6. CT zoomed in around Bragg peak locations for oblique beams, showing results from SNR = 0dB simulations. Bragg peak locations for "control" beams and "measured" beam #5 are plotted with magenta squares and dot, respectively. Dotted yellow lines connect the transducer locations to the beamformed estimate (yellow triangle). A dashed line connects the beamformed estimate to the nearest control point, and a solid yellow line connects the control point to the final estimate (yellow circle). [Color figure can be viewed at wileyonlinelibrary.com]

In principle, if the thermoacoustic source were a single point then triangulation would require only three transducer locations and distances to the Bragg peak to localize the Bragg peak at $\mathbf{x} = (x,y,z)$ by solving for each transducer location $\mathbf{x}_k = (x_k,y_k,z_k)$

$$|\mathbf{x} - \mathbf{x}_k|^2 = D_k^2 \qquad \text{for } k = 1, 2, 3, \ldots N$$

where v_s represents soundspeed and N is the number of transducer locations.

We used four transducer locations for this simulation study, and solved in a least-square sense by first linearizing the system of quadratic equations. Subtracting for $j \neq k$ yielded $6 = N(N-1)/2$ linear equations

$$2\mathbf{x} \cdot (\mathbf{x}_k - \mathbf{x}_j) = (|\mathbf{x}_k|^2 - |\mathbf{x}_j|^2) - (D_k^2 - D_j^2) \qquad (2)$$

All parameters were known except for the desired Bragg peak location, and a least squares solution, $\mathbf{x}_{LSQ}$, was found.

For arbitrary transducer locations the least squares solution is unique, but coplanar transducer locations led to a rank-deficient linear system. The least-squares solution was orthogonal to the transducer plane, i.e., $\mathbf{x} = \mathbf{x}_{LSQ} + c\mathbf{n}$, with $\mathbf{n} = (0,0,1)$ the unit normal to the coronal transducer plane. The normal component was determined by returning to the original nonlinear equations

TABLE IV. Beam range to Bragg peak, distance to center of transducer aperture, and errors for beamformed estimates. All are reported in millimeters.

			Errors, noise-free		Average Errors, SNR = 0 dB	
Run name	Beamlet range	Dist 2 transd	Beamformed	Final	Beamformed	Final
Oblique 3	117	25	5.0	0.3	5.2	1.5
Oblique 5	110	31	8.1	0.8	8.9	1.5
Oblique 7	102	36	8.8	1.0	9.0	2.0
Lateral 2	148	26	4.6	1.6	5.2	1.9

$$|\mathbf{x}_{LSQ} + c\mathbf{n} - \mathbf{x}_k|^2 = D_k^2 \tag{3}$$

and expanding to get k quadratic equations with respect to c,

$$c^2 + 2\mathbf{n} \cdot \mathbf{x}_k c + [|\mathbf{x}_{LSQ} - \mathbf{x}_k|^2 - D_k^2] = 0 \tag{4}$$

The quadratic formula yielded two solutions, $c_{k\pm}$, to each equation. For each k, one of the solutions was incorrect. For the transducer geometry we consider, least-squares solutions were in the coronal plane located 28 mm posterior, so desired solutions were given by elevating the least squares solution by c_{k+}. If the distances $\{D_k\}$ were updated accurately, then the $\{c_{k+}\}$ would be identical for noise-free simulations. In practice, we found that the $\{c_{k+}\}$ were very nearly equal for noise free simulations. The average was taken to estimate $c_{LSQ} = mean\{c_{k+}\}$. As additive noise increased, the discriminant in Eq. (4) was sometimes negative, resulting in complex-valued solutions. Therefore, the real part was used to estimate c_{LSQ} and $\mathbf{x} = \mathbf{x}_{LSQ} + c_{LSQ}\,\mathbf{n}$.

3. RESULTS

Beam range and mean distance between Bragg peak and receive transducers is compared to range error for both noise-free and noisy data in Table IV. Final estimates were more accurate than beamformed estimates and were robust to white noise. Range errors computed from noise-free and SNR = 0 dB data were no more than 1.6 mm or and 2.0 mm respectively. Coordinates for beamformed and final estimates from noise-free data are tabulated in the Appendix.

For oblique beams, errors increased with distance between Bragg peak and transducer, i.e., distance covered in taking the first step. For small beam angles, therefore, errors are expected to decrease with beam range and complement current range errors that are proportional to the range.

4. DISCUSSION

Ionoacoustic range verification offers the possibility of providing online range verification with direct correlation to underlying anatomy. This study introduces a two-step range verification algorithm that leverages Monte Carlo and acoustic simulations based upon volumetric computerized tomography (VCT) to robustly and accurately estimate range from lowpassed and noisy thermoacoustic emissions, accounting for the proton pulse envelope without resorting to deconvolution,[33] which is a notoriously unstable operation. Clinical implementation for treating prostate cancer would replace the rectal balloon, an immobilization device to restrict intrafractional motion of prostate and reduce rectum dose, with a custom transrectal array and co-register live ultrasound images to VCT. Treatment plans would eliminate the degree 180 beam to avoid irradiating the ultrasound array. Online operation will require fast recomputation of thermoacoustic emissions, either by GPU-based Monte Carlo[41] and acoustic simulation, or by correcting precomputed emissions. We envision that clinical implementation of ionoacoustic range verification for proton therapy would avoid catastrophic range errors and provide enough information to recalculate the true dose delivered to patients.[42]

Coregistration errors are expected to limit accuracy of the method, rather than numerical errors, as discussed in subsection 4.A. Challenges to ionoacoustic range verification include developing acoustic hardware with both ultrasound imaging arrays and also low-frequency receive elements that are sensitive to thermoacoustic emissions, which are both low frequency and low amplitude, as discussed in Subsection 4.B. Suitable applications will permit ultrasound imaging of the target volume, ideally with transducers placed distal to the Bragg peak on a measurement aperture nearly perpendicular to the beamline. Limited angle streak artifacts in beamformed volumes will then run approximately perpendicular to the beamline, pinpointing the Bragg peak location.

Limitations of this study are failure to account for transducer response, acoustic attenuation, and enhanced signal generation by the gold fiducials. When transducer frequency response is known, it should be convolved against the simulated emissions, just as the proton pulse envelope was in Section 2.D. Attenuation of low frequency thermoacoustic emissions is expected to be a minor effect, and k-Wave software could account for it. However, applying the Grüneisen and density of gold to Viscoil fiducial voxels added delta-functions to the initial pressure map. Although k-Wave managed discontinuities at tissue interfaces the extremely high frequency content due to fiducials was too much for k-Wave's standard implementation of the pseudospectral method. More sophisticated, and likely computationally costly, acoustic modeling may be required to handle fiducials.

Overlays of range estimates onto live ultrasound images are inherently robust to soundspeed inhomogeneity because US images created by two-way beamforming suffer similar errors as one-way beamformed range estimates. In the Supplemental Material registration errors due to dispersion are discussed and a simple pitch-catch experiment demonstrates that overlay of a one-way beamformed range estimate is robust relative to the ultrasound image, despite deformation due to acoustic heterogeneity.

4.A. Limitations on accuracy of final estimates

Although beamformed range estimates are inherently coregistered to ultrasound images their accuracy is limited by frequency content of thermoacoustic emissions. Control points with known distance to each receive transducer can be used to overcome the errors in beamformed estimates by accurately estimating the distance between receive transducers and desired Bragg peak location. Triangulation is then performed via linear least squares to estimate the Bragg peak location more accurately than the beamformed estimates. Baseline accuracy of final range estimates is limited by the accuracy of control data simulated using Monte Carlo and acoustic propagation software. Numerical errors are likely to be small compared to interfraction positioning errors and anatomical changes, so we expect that the control database should be recomputed daily.

Interpreted Matlab code computed beamformed and final range estimates in approximately 750 and 10 ms, respectively, when a control database was already available. Total runtime for nonoptimized Monte Carlo and k-wave simulations exceeded 40 min per beamlet. However, GPU acceleration of image registration (planning CT onto daily ultrasound), Monte Carlo dose calculations, and k-Wave acoustic models could someday reduce computation times sufficiently for online operation.

4.B. Custom US probes will be required for ionoacoustic range verification

To ensure robustness to soundspeed inhomogeneity, thermoacoustic receive elements should be colocated with pulse-echo imaging elements. But thermoacoustic signals are lower frequency and weaker than pulse-echoes, so different transducer materials and dimensions may be required to detect thermoacoustic emissions. Finally, ion therapy vaults are harsh environments for electronics, and possibly transducer materials.

Pulse echoes used to generate ultrasound images have carrier frequencies above 1 MHz, whereas thermoacoustic emissions are bandlimited well below 1 MHz as shown in Fig. 4(c). Additionally, thermoacoustic emissions are weak. Clinical synchrocyclotrons deliver on the order of 10 pC/pulse and transducers are located several cm from the Bragg peak, so amplitudes of detected pressures will be on the order of 100 mPa [Figs. 3 and 4(b)], which is low compared to the noise-equivalent-pressure of standard ultrasound imaging arrays.

Furthermore, secondary emissions (neutrons, prompt gamma) and also electromagnetic interference (EMI) can damage hardware and corrupt data. EMI is routinely handled very well by ultrasound systems with diodes that do not conduct when voltage exceeds a threshold. Data corresponding to the first few microseconds after ion delivery may be lost, which for this application means Bragg peak locations within 5 mm of the transducer may be difficult to recover. If piezoelectric crystals prove susceptible to damage from secondary emissions, then amorphous transducer materials will be required.

In summary, incorporating small, radiation-hard elements that are sensitive to very low frequencies onto the form factors of ultrasound imaging arrays will be required for clinical operation.

5. CONCLUSIONS

Beam range was estimated with average errors of 2.0 mm or less, even with SNR 0 dB. Accuracy at this level is substantially less than the distal margin currently used in treatment planning, which is 3.5% of the proton range plus 3 mm. Online implementation in clinical practice could improve confidence in delivery up to the accuracy of thermoacoustic verification. When overlaid on live ultrasound images, ionoacoustic range verification could be used to correct for setup uncertainty and intrafractional motion.

Online beamformed range verification for distal transducer locations will be feasible if weak thermoacoustic emissions can be detected with adequate SNR. Commercial ultrasound systems that provide automated beam gating during x-ray radiation therapy are prime candidates for adaptation to online range verification during proton therapy.

Final estimates are more accurate than beamformed estimates, and could enable adaptive planning to compensate for range errors during subsequent fractions. In future, accelerated Monte Carlo and acoustic simulations may enable online execution.

ACKNOWLEDGMENTS

The authors thank Jeff Heine and Patrick Zerkel for assistance in measuring the temporal characteristics on the Mevion S250. S.K.P. thanks Ted Lynch of CIRS, Inc. for providing tissue-mimicking samples.

CONFLICT OF INTEREST

The authors have no relevant conflicts of interest to disclose.

APPENDIX

Coordinates for Bragg peak locations are tabulated below. True Bragg peak locations are listed in column two, beamformed and final estimates from noise-free data are listed in columns three and four.

TABLE A1. Bragg peak true and estimated coordinates in millimeters.

Run name	Bragg peak (●) (LR AP SI)	Beamform (Δ) (LR AP SI)	Beamform error (Δ)	Final (O) (LR AP SI)
Oblique 2	(−1 7 118)	(−1 4 120)	2.4	

A). Continued.

Run name	Bragg peak (●) (LR AP SI)	Beamform (Δ) (LR AP SI)	Beamform error (Δ)	Final (O) (LR AP SI)
Oblique 3	(2 4 118)	(2 1 122)	5.0	(1.9 4.2 117.8)
Oblique 4	(5 1 118)	(4 −3 122)	5.7	
Oblique 5	(8 −2 117)	(6 −6 124)	8.1	(8.6 −0.8 117.4)
Oblique 6	(11 −5 118)	(10 −9 126)	9.5	
Oblique 7	(14 −7 118)	(18 −12 124)	8.8	(13.6 −7.4 117.2)
Oblique 8	(17 −10 118)	(21 −15 121)	6.9	
Lateral 1	(11 2 111)	(16 1 110)	5.2	
Lateral 2	(7 2 112)	(11 1 110)	4.6	(8.4 2.3 111.4)
Lateral 3	(3 2 110)	(8 1 111)	5.2	

[a]Author to whom correspondence should be addressed. Electronic mail: patchs@uwm.edu; Telephone: +1 414 229 4475.

REFERENCES

1. ASTRO. *American Society for therapeutic radiology and oncology – Model policies, proton beam therapy (PBT)*; 2014. http://www.astro.org/uploadedFiles/Main_Site/Practice_Management/Reimbursement/ASTRO%20PBT%20Model%20Policy%20FINAL.pdf.
2. Knopf AC, Lomax A. In vivo proton range verification: a review. *Phys Med Biol*. 2013;58:R131–R160.
3. Hoesl M, Deepak S, Moteabbed M, et al. Clinical commissioning of an in vivo range verification system for prostate cancer treatment with anterior and anterior oblique proton beams. *Phys Med Biol*. 2016;61:3049.
4. Dendooven P, Buitenhuis HJ, Diblen F, et al. Short-lived positron emitters in beam-on PET imaging during proton therapy. *Phys Med Biol*. 2015;60:8923–8947.
5. Frey K, Unholtz D, Bauer J, et al. Automation and uncertainty analysis of a method for in-vivo range verification in particle therapy. *Phys Med Biol*. 2014;59:5903–5919.
6. Cambraia Lopes P, Clementel E, Crespo P, et al. Time-resolved imaging of prompt-gamma rays for proton range verification using a knife-edge slit camera based on digital photon counters. *Phys Med Biol*. 2015;60:6063–6085.
7. Min CH, Lee HR, Kim CH, Lee SB. Development of array-type prompt gamma measurement system for in vivo range verification in proton therapy. *Med Phys*. 2012;39:2100–2107.
8. Min C-H, Kim C, Youn M-Y, Kim J-W. Prompt gamma measurements for locating the dose falloff region in the proton therapy. *Appl Phys Lett*. 2006;89:183517.
9. Polf JC, Avery S, Mackin DS, Beddar S. Imaging of prompt gamma rays emitted during delivery of clinical proton beams with a Compton camera: feasibility studies for range verification. *Phys Med Biol*. 2015;60:7085–7099.
10. Polf JC, Mackin D, Lee E, Avery S, Beddar S. Detecting prompt gamma emission during proton therapy: the effects of detector size and distance from the patient. *Phys Med Biol*. 2014;59:2325–2340.
11. Verburg JM, Riley K, Bortfeld T, Seco J. Energy- and time-resolved detection of prompt gamma-rays for proton range verification. *Phys Med Biol*. 2013;58:L37–L49.
12. Verburg JM, Seco J. Proton range verification through prompt gamma-ray spectroscopy. *Phys Med Biol*. 2014;59:7089–7106.
13. Verburg JM, Testa M, Seco J. Range verification of passively scattered proton beams using prompt gamma-ray detection. *Phys Med Biol*. 2015;60:1019–1029.
14. Hu Y, Rankine L, Green OL, et al. Characterization of the onboard imaging unit for the first clinical magnetic resonance image guided radiation therapy system. *Med Phys*. 2015;42:5828–5837.
15. Saenz DL, Yan Y, Christensen N, et al. Characterization of a 0.35T MR system for phantom image quality stability and in vivo assessment of motion quantification. *J Appl Clin Med Phys*. 2015;16:5353.
16. Askariyan GA, Dolgoshein BA, Kalinovsky AN, Mokhov NV. Acoustic detection of high energy particle showers in water. *Nucl Instrum Methods*. 1979;164:267–278.
17. Sulak L, Armstrong R, Baranger H, et al. Experimental Studies of the Acoustic Signature of Proton Beams Traversing Fluid Media. *Nucl Instrum Methods*. 1979;161:203–217.
18. Tada J, Hayakawa Y, Hosono K, Inada T. Time resolved properties of acoustic pulses generated in water and in soft tissue by pulsed proton beam irradiation-A possibility of doses distribution monitoring in proton radiation therapy. *Med Phys*. 1991;18:1100–1104.
19. Hayakawa Y, Tada J, Arai N, et al. Acoustic Pulse Generated in a Patient During Treatment by Pulsed Proton Radiation Beam. *Radiat Oncol Investig*. 1995;3:42–45.
20. Jones KC, Witztum A, Sehgal CM, Avery S. Proton beam characterization by proton-induced acoustic emission: simulation studies. *Phys Med Biol*. 2014;59:6549–6563.
21. Ahmad M, Xiang L, Yousefi S, Xing L. Theoretical detection threshold of the proton-acoustic range verification technique. *Med Phys*. 2015;42:5735.
22. Alsanea F, Moskvin V, Stantz KM. Feasibility of RACT for 3D dose measurement and range verification in a water phantom. *Med Phys*. 2015;42:937–946.
23. Xiang L, Han B, Carpenter C, Pratx G, Kuang Y, Xing L. X-ray acoustic computed tomography with pulsed x-ray beam from a medical linear accelerator. *Med Phys*. 2013;40:10701.
24. Xiang L, Tang S, Ahmad M, Xing L. High Resolution X-ray-Induced Acoustic Tomography. *Sci Rep*. 2016;6:26118.
25. Assmann W, Kellnberger S, Reinhardt S, et al. Ionoacoustic characterization of the proton Bragg peak with submillimeter accuracy. *Med Phys*. 2015;42:567–574.
26. Kellnberger S, Assmann W, Lehrack S, et al. Ionoacoustic tomography of the proton Bragg peak in combination with ultrasound and optoacoustic imaging. *Sci Rep*. 2016;6:29305.
27. Jones KC, Vander Stappen F, Bawiec CR, et al. Experimental observation of acoustic emissions generated by a pulsed proton beam from a hospital-based clinical cyclotron. *Med Phys*. 2015;42:7090.
28. Lehrack S, Assmann W, Bertrand D, et al. Submillimeter ionoacoustic range determination for protons in water at a clinical synchrocyclotron. *Phys Med Biol*. 2017;62:L20.
29. Patch S, Kireeff-Covo M, Jackson A, et al. Thermoacoustic Range Verification using a Clinical Ultrasound Array Provides Perfectly co-Registered Overlay of the Bragg peak onto an Ultrasound Image. *Phys Med Biol*. 2016;61:5621–5638.
30. Polf J, Parodi K. Imaging particle beams for cancer treatment. *Phys Today*. 2015;68:28–33.
31. Anastasio M, Zhang J, Modgil D, La Rivière PJ. Application of inverse source concepts to photoacoustic tomography. *Inverse Probl*. 2007;23:S21–S36.
32. Henrotin S, Abs M, Forton E, et al. *Commissioning and testing of the first IBA S2C2*. In 2015:TUP07.
33. Jones KC, Vander Stappen F, Sehgal CM, Avery S. Acoustic time-of-flight for proton range verification in water. *Med Phys*. 2016;43:5213.
34. Giebeler A, Fontenot J, Balter P, Ciangaru G, Zhu R, Newhauser W. Dose perturbations from implanted helical gold markers in proton therapy of prostate cancer. *J Appl Clin Med Phys*. 2009;10:2875.
35. Perl J, Shin J, Schumann J, Faddegon B, Paganetti H. TOPAS: an innovative proton Monte Carlo platform for research and clinical applications. *Med Phys*. 2012;39:6818–6837.
36. Schneider W, Bortfeld T, Schlegel W. Correlation between CT numbers and tissue parameters needed for Monte Carlo simulations of clinical dose distributions. *Phys Med Biol*. 2000;45:459–478.
37. Treeby BE, Cox BT. k-Wave: MATLAB toolbox for the simulation and reconstruction of photoacoustic wave-fields. *J Biomed Opt*. 2010;15:21314.
38. Duck F. *Physical Properties of Tissue*. London, San Diego: Academic Press; 1990.
39. Xu M, Wang LV. Universal back-projection algorithm for photoacoustic computed tomography. *Phys Rev E*. 2005;71:16706.

40. Patch SK. Thermoacoustic tomography-consistency conditions and the partial scan problem. *Phys Med Biol*. 2004;49:2305–2315.
41. Jia X, Schumann J, Paganetti H, Jiang SB. GPU-based fast Monte Carlo dose calculation for proton therapy. *Phys Med Biol*. 2012;57: 7783–7797.
42. Jaffray DA, Lindsay PE, Brock KK, Deasy JO, Tome WA. Accurate accumulation of dose for improved understanding of radiation effects in normal tissue. *Int J Radiat Oncol Biol Phys*. 2010;76(3 Suppl):S135–S139.

SUPPORTING INFORMATION

Additional Supporting Information may be found online in the supporting information tab for this article.

Fig. S1: Phase velocities computed according to Eq. (S1) in black; fitted to measurements in color. Solid thick lines represent experimentally corroborated ultrasound regime; solid dashed lines represent the thermoacoustic regime.

Fig. S2: Data and results from pitch-catch experiments through water.

Fig. S3: Data and results from pitch-catch experiments through acoustic heterogeneities: tissue mimicking gelatin phantom and 5 mm bone mimicking slab.

Fig. S4: Zoomed in data and results displayed on the same grayscales. Pitch-catch signals through water (a) and inhomogeneities (b). Backprojected images through water (c) and inhomogeneities (d).

Fig. S5: B-mode images of single element transducer imaged through water and inhomogeneous field overlaid in green and red respectively.

Supplemental Material

Overlays of range estimates onto ultrasound images are inherently robust to soundspeed variations

Commercial systems accurately co-register photoacoustic and ultrasound images, and we examine below factors that might introduce registration errors in thermoacoustic range verification: soundspeed variations due to dispersion and spatial inhomogeneity. Firstly, propagation speeds of low frequency thermoacoustic emissions are expected to be lower than propagation speeds of pulse echoes used to generate B-mode ultrasound images. Secondly, acoustic propagation paths traversed during two-way beamforming can differ from one-way propagation trajectories from an acoustic source to receiver. Ultrasound pulse echoes could, in principle, experience very different refraction effects than thermoacoustic emissions, resulting in registration errors. In this supplemental document we provide a brief review of early literature on acoustic dispersion, starting with PNT Wells' assertion that "dispersion is small, and usually negligible in relation to variations and uncertainties of measurement[1]." We also provide an example demonstrating the minimal effect of differing acoustic paths through homogeneous and also inhomogeneous media containing a strong scatterer.

Clinical ultrasound imaging systems rely upon the assumption that soundspeed is uniform, and ultrasound images suffer deformation and blurring as a result of soundspeed inhomogeneity. Nevertheless, ultrasound is an effective clinical tool in most soft tissues. Dispersion is significant in bone and lung[2], but ultrasound imaging does a poor job in each case so they are outside the recommended scope of our method. Dispersion has been studied in more papers than can be cited here but we mention a few early references. O'Donnell, Jaynes & Miller pointed out that attenuation and dispersion are related to each other via Kramers-Kronig relations, which rely only upon causality rather than specific acoustic properties of the media[3]. Defining the wave vector as $k = \frac{\omega}{C(\omega)} + i\,\alpha(\omega)$, where α and C represent attenuation coefficient and soundspeed, and assuming $\alpha(\omega)\,C(\omega) \ll \omega$, they developed a local (differential) dispersion relation:

$$\frac{dC(\omega)}{d\omega} = \frac{2\,C_o^2}{\pi\,\omega^2}\alpha(\omega) \qquad \text{(S1)}$$

Attenuation in soft tissue typically follows a power law model of the form, $\alpha(\omega) = a\omega^b$. Applying values representative of highly attenuative tissue, $b = 1.1$ and $a = 0.1\ Np\ cm^{-1}\ MHz^{-b}$, and integrating Eq. S1 assuming $\omega_o = 1\ MHz$ and $C_o = 1.54\ mm/\mu s$ yields the black dispersion curve in Fig. 1. Phase velocity varies by less than 6% over three decades from 10 kHz to 10 MHz.

Sehgal & Greenleaf modeled absorption due to relaxation as a function of measured relaxation times and specific heat ratio, fit measured data to their model, and then utilized Eq. S1 to express soundspeed as a function of relaxation times, specific heat ratio, and frequency[4]. Phase velocities computed according to Eq. 38 and parameters in Table 1 from[4], again assuming $\omega_o = 1\ MHz$, are plotted in color in Fig. 1. Note that soundspeed variation in the black dispersion curve for highly attenuative tissue is comparable to soundspeed differences between tissue types.

Many experimental reports corroborate Eq. S1 for soft tissues above 1 MHz but relatively few measurements have been reported at kHz frequencies. Measuring phase velocities in human tissues over the frequency range relevant to thermoacoustic emissions may be required for accurate co-registration of thermoacoustic range estimates to ultrasound images.

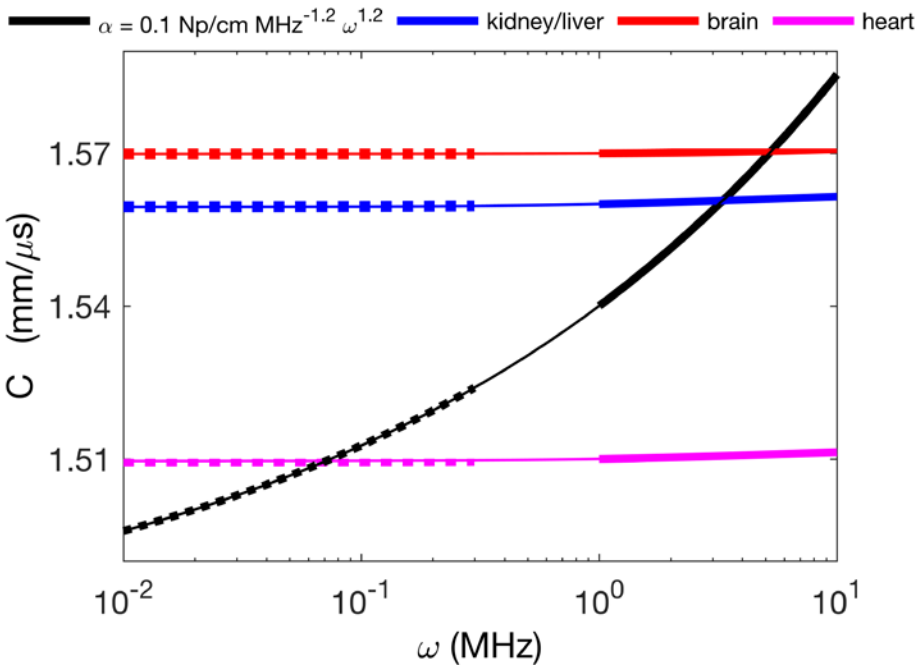

Fig. 1. Phase velocities computed according to Eq. S1 in black; fitted to measurements in color. Solid thick lines represent experimentally corroborated ultrasound regime; solid dashed lines represent the thermoacoustic regime.

Registration errors due to dispersion are expected to be on the same order as errors due to soundspeed variations with respect to tissue type.

Acoustic propagation path differences have not hindered overlays of photoacoustic images onto ultrasound images. The next two pages describe an acoustic source experiment demonstrating that co-registration of range estimates onto US images is inherently robust to acoustic spatial inhomogeneity. We overlaid a one-way beamformed, or backprojected, image of a pulse transmitted by a single element transducer onto ultrasound images that visualized the transducer. A 2.25 MHz single element transducer (Olympus V306) excited by a pulser-receiver (Olympus 5900PR) mimicked a proton beam as acoustic source. A P4-1 *phased* array with center frequency 2.5 MHz received the transmitted pulses, which were amplified and saved to disk by a Verasonics V1 system. Because transmit and receive frequencies were similar, dispersion was removed as a variable. B-mode images were acquired immediately prior to each pitch-catch experiment using Verasonics' "WideBeam" script, which fires all 96 channels for each transmit pulse. Images are created by combining dozens of pulse echoes generated with different transmit delays in order to interrogate tissue along divergent rays. Paths traversed by pulse echoes are not identical to the unidirectional paths traversed by thermoacoustic emissions, but refraction of pulse echoes is mimicked by refraction in the pitch-catch experiments as demonstrated below.

Experiments were performed with only room temperature water between transducers in the control case; a tissue mimicking gelatin block[6] and 5 mm bone sample (CIRS DCB-403B) were placed between transducers to examine the effect of acoustic heterogeneity on both B-mode and backprojected images.

Figs. 2 and 3 display data and results for the homogeneous control and heterogeneous acoustic fields, respectively. Subfigures (a) display the pitch-catch measurements as measured by all 96 channels of the phased array. Subfigures (b) display the one-way beamformed images created from data in (a). Display windows for (a) and (b) subfigures have 80% window width compared to MATLAB's native display. Images in subfigures (c) were collected with different transmit-gain settings to optimize image quality. Inset subfigures (d) zoom in on the single element transducer in (c), with a threshholded version of (b) overlaid in yellow.

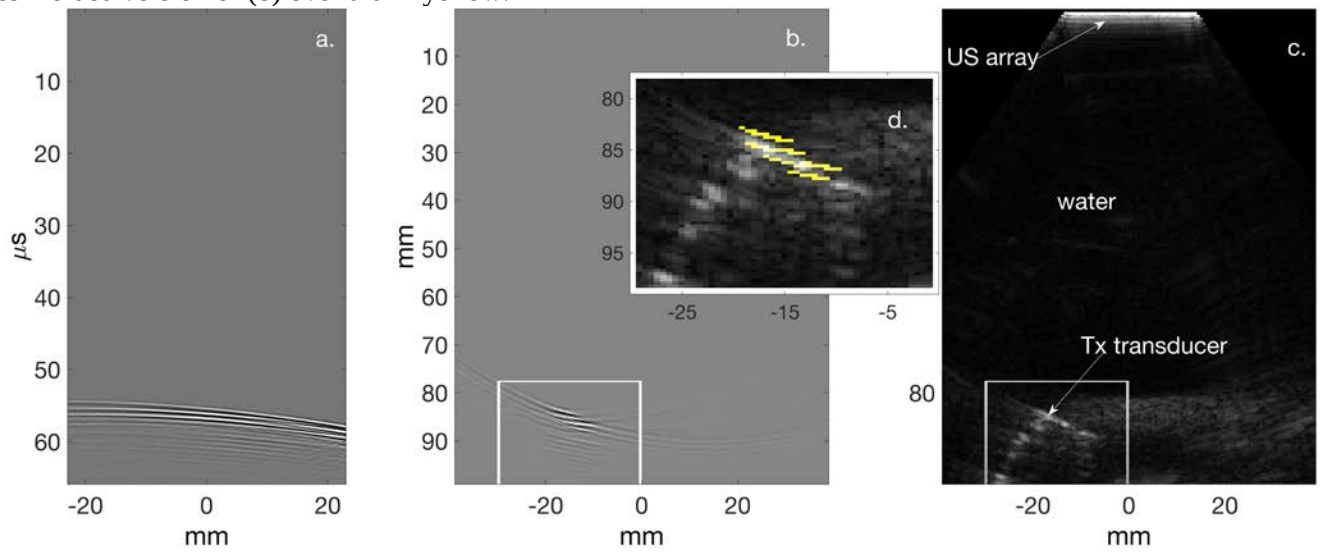

Fig 2. Data and results from pitch-catch experiments through water.

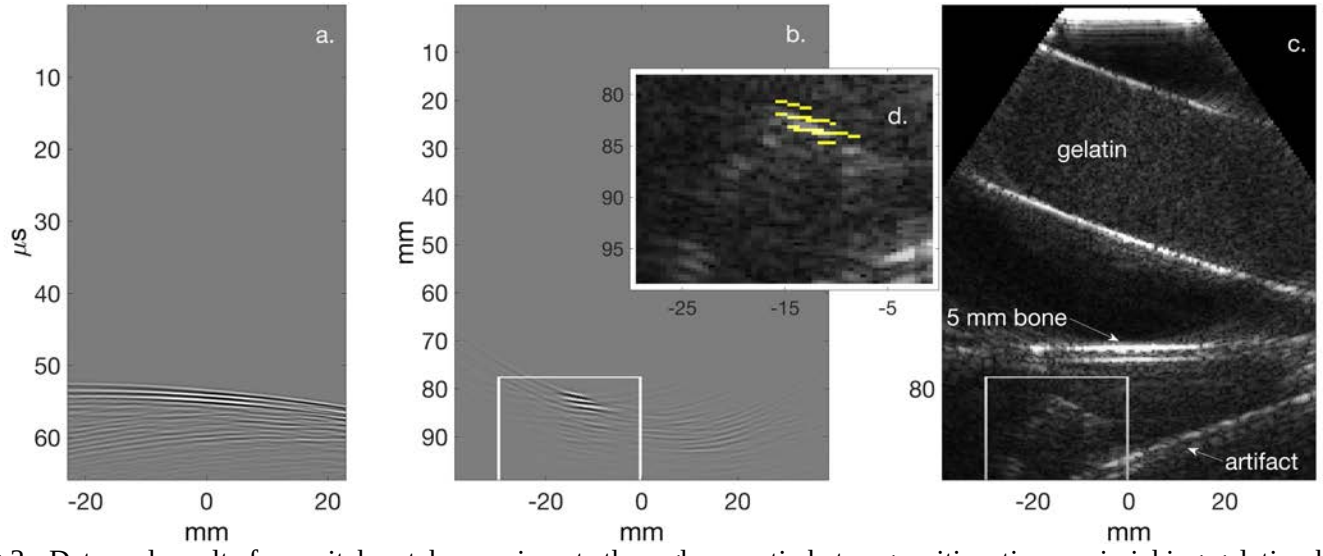

Fig 3. Data and results from pitch-catch experiments through acoustic heterogeneities: tissue mimicking gelatin phantom and 5 mm bone mimicking slab.

Comparing pitch-catch datasets reveals differences in arrival times and amplitudes. Increased propagation speeds in the gelatin and 5 mm bone sample shifted one-way times of flight by approximately $2\,\mu s$, as shown by comparing subfigures (a) and (b) in Fig. 4, where results are displayed using the same greyscale to highlight attenuation due to the presence of acoustic scatterers. Accordingly, backprojected images display constructive interference at depths that differ by about 3 mm in subfigures (c) and (d). B-mode images of the single element transducer were similarly affected, as can be seen by comparing the red and green images in Fig. 5. The upper corner of the transducer moved from (83.5 mm, -17.4 mm) = (depth, lateral) coordinates to (81 mm, -14.5 mm).

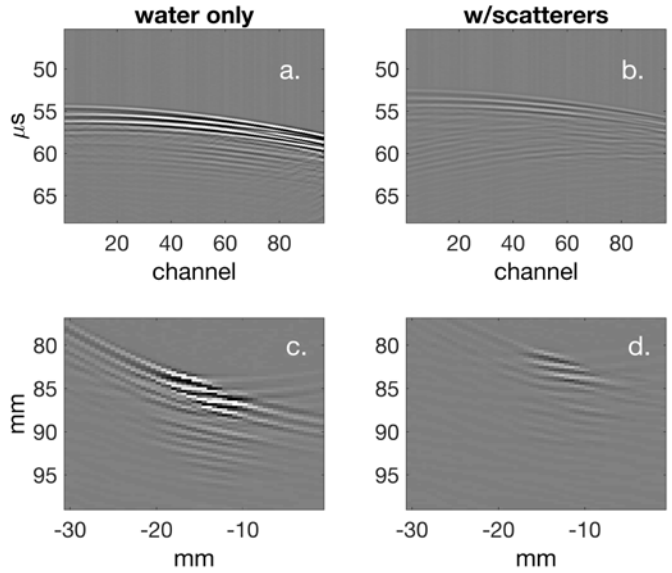

Fig. 4. Zoomed in data and results displayed on the same greyscales. Pitch-catch signals through water (a) and inhomogeneities (b). Backprojected images through water (c) and inhomogeneities (d).

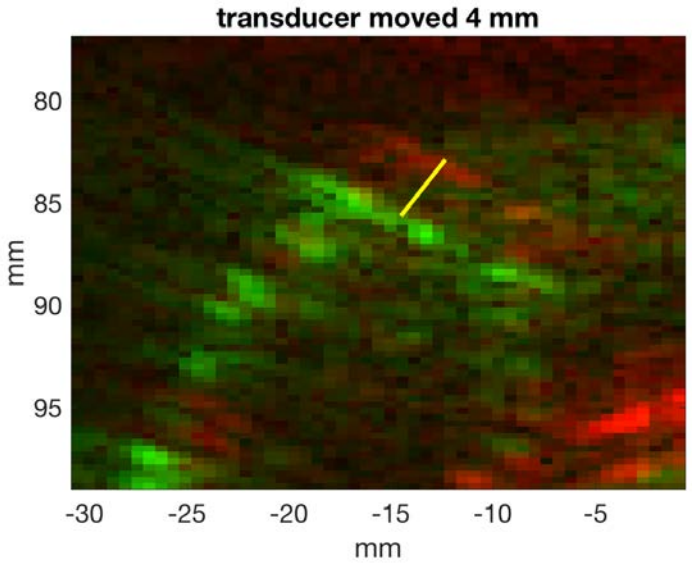

Fig. 5. B-mode images of single element transducer imaged through water and inhomogeneous field overlaid in green and red, respectively.

Because pulses with a clear carrier frequency were transmitted, destructive interference yielded far better lateral resolution in backprojected images than might be expected from the limited angle measurement aperture of the P4-1 array. Backprojecting deconvolved projections – or thermoacoustic emissions - yields streak artifacts similar to those seen in x-ray CT. The range can be estimated as the intersection of the streak artifact with the known ion beam trajectory, as was done in[7].

Although absolute coordinates of thermoacoustic range estimates may be affected by acoustic inhomogeneity, overlays will be accurate relative to the ultrasound image of underlying anatomy.

Supplemental References

1. Wells PNT. Absorption and dispersion of ultrasound in biological tissue. Ultrasound in Medicine and Biology. 1(4):369–376.
2. Duck F. Physical Properties of Tissue. London, San Diego: Academic Press; 1990.
3. O'Donnell M, Jaynes ET, Miller JG. General relationships between ultrasonic attenuation and dispersion. The Journal of the Acoustical Society of America. 1978 Jun 1;63(6):1935–1937.
4. Sehgal CM, Greenleaf JF. Ultrasonic absorption and dispersion in biological media: A postulated model. The Journal of the Acoustical Society of America. 1982 Dec 1;72(6):1711–1718.
5. Truong XT, Jarrett SR, Rippel DV. Longitudinal pulse propagation characteristics in striated muscle. The Journal of the Acoustical Society of America. 1978 Nov 1;64(5):1298–1302.
6. Lazebnik M, Madsen EL, Frank GR, Hagness SC. Tissue-mimicking phantom materials for narrowband and ultrawideband microwave applications. Physics in Medicine and Biology. 2005;50(18):4245–4528.
7. Patch S, Kireeff-Covo M, Jackson A, Qadadha Y, Campbell K, Albright R, Bloemhard P, Donoghue A, Siero C, Gimpel T, Small S, Ninemire B, Johnson M, Phair L. Thermoacoustic Range Verification using a Clinical Ultrasound Array Provides Perfectly co-Registered Overlay of the Bragg peak onto an Ultrasound Image. Physics in Medicine and Biology. 2016;61:5621–5638.